UNIVERSITY OF CALIFORNIA SAN DIEGO

The Effect of Vinculin Deletion on Myofilament Architecture and the Implications for Systolic Force Generation in the Heart

A thesis submitted in partial satisfaction of the requirements

for the degree Master of Science

in

Bioengineering

by

Matthew Scott Janssen

Committee in charge:

Professor Jeffrey H. Omens, Chair
Professor Andrew D. McCulloch
Professor Robert S. Ross

2011

The Thesis of Matthew Scott Janssen is approved and it is acceptable in quality and form for publication on microfilm and electronically:

Chair

University of California, San Diego

2011

To the cherished memory of my cousin Maria

TABLE OF CONTENTS

LIST OF FIGURES

LIST OF TABLES

ACKNOWLEDGEMENTS

This thesis represents a portion of one year of research within the Cardiac Mechanics Research Group (CMRG) in the Department of Bioengineering at the University of California, San Diego. First, I would like to thank my advisors Dr. Jeffrey Omens and Dr. Andrew McCulloch for their guidance and assistance throughout my research. I would also like to thank Dr. Robert Ross for providing the vinculin-knockout mice as well as his constructive criticism.

I would like to extend my gratitude to the National Center for Microscopy and Imaging Research (NCMIR) for allowing me to utilize their electron microscopes and equipment. In particular, I would like to thank Masahiko Hoshijima for preparing my tissue samples for use with EM; in addition, I would like to acknowledge Mason Mackey, Tomas Molina, and Masako Terada for taking the time to offer their expertise and train me in the essential processes for my project. I would also like to extend my gratitude to Dr. Ron Milligan and Reza Khayat at Scripps Research Institute; their help with Fourier transforms proved to be crucial to my image processing.

I would like to thank my colleagues in CMRG, especially Jared Tangney for his collaboration and assistance with developing the computational model; his expertise helped me develop significant conclusions from my measurements. Furthermore, I would like to acknowledge Brianna Potter and Taylor Coe for their help behind the scenes in organizing the transfer of mice from the VA San Diego Medical Center.

I would like to thank my family and friends for always being there. I would like to extend my dearest gratitude to my parents for their unwavering support and inspiration in all of my endeavors; without them, I would not be the person that I am today. Finally, I would like to thank the love of my life, my fiancé Jill, for staying by my side throughout the entire process and keeping me grounded; her support and encouragement kept me motivated and helped me keep everything in perspective.

Chapter 1, in part, is currently being prepared for submission for publication of the material. Chuang J; Janssen MS; Tangney J; Liao P; Ross RS; McCulloch AD; Omens JH. "The Role of Vinculin in Active Fiber and Sheet Mechanics." The thesis author was the secondary investigator and author of this material.

Chapter 2, in part, is currently being prepared for submission for publication of the material. Chuang J; Janssen MS; Tangney J; Liao P; Ross RS; McCulloch AD; Omens JH. "The Role of Vinculin in Active Fiber and Sheet Mechanics." The thesis author was the secondary investigator and author of this material.

Chapter 3, in part, is currently being prepared for submission for publication of the material. Chuang J; Janssen MS; Tangney J; Liao P; Ross RS; McCulloch AD; Omens JH. "The Role of Vinculin in Active Fiber and Sheet Mechanics." The thesis author was the secondary investigator and author of this material.

ABSTRACT OF THE THESIS

The Effect of Vinculin Deletion on Myofilament Architecture and the Implications for Systolic Force Generation in the Heart

by

Matthew Scott Janssen

Master of Science in Bioengineering

University of California, San Diego, 2011

Professor Jeffrey H. Omens, Chair

Vinculin (Vcl) is a membrane-associated protein that has been shown to play key structural roles in cell adhesion sites and may affect myocardial mechanical function in a direction-dependent manner. Previous studies measured the mechanical effects of Vcl disruption using tagged magnetic resonance imaging (MRI) *in vivo* and reported significant decreases in the transverse systolic strain components in a

cardiomyocyte-specific vinculin knockout (cVclKO) mouse model compared with littermate controls [1]. However, there was no change in systolic fiber strain *in vivo* [1]. One possible mechanism might be alterations in sarcomeric structure; thus, the lattice spacing and sarcomere length were measured in fixed hearts using microscopy. Measurements from optical diffraction patterns generated using FFTs of electron micrographs yielded an average normalized lattice spacing of 0.0113±0.001 (SD) in end-diastolic cVclKO hearts *vs.* 0.0095±0.001 in controls ($P<0.05$, $n=3$). A similar trend was observed in the barium-contracted hearts. A crossbridge model was used to compute changes in transverse and axial crossbridge forces associated with this increase in myofilament lattice spacing. A finite element model incorporating these changes in systolic material properties recapitulated key mechanical differences seen between control and mutant mice. The results suggest that Vcl ablation increased myofilament lattice spacing, which alters the crossbridge binding angle of myosin heads; this, in turn, increases the transverse component of sarcomere force and consequently decreases systolic cross-fiber strains *in vivo*. These results with the experimental measurements suggest that Vcl can influence myofilament architecture and systolic force generation in a direction-dependent manner.

Chapter 1

General Introduction

1.1 STRUCTURE OF CARDIOMYOCYTES

Normal myocardial function is strongly dependent on the structure of the cardiomyocytes. The ultrastructure of these cells contains several significant components, which include but are not limited to the sarcomere, costamere, and intercalated disc. The structure from Z-disc to Z-disc of a myofibril is called the sarcomere, and it is the basic contractile unit of the cardiomyocyte; these structures are comprised of thick and thin filaments, which are made of mostly myosin and actin, respectively [2]. The thick and thin filaments are arranged in complimentary hexagonal arrays [2] as shown in Figure 1.1; the interaction between the two is the basis for muscle contraction.

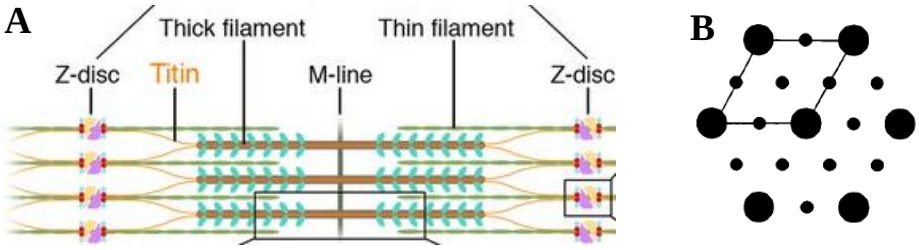

Figure 1.1: (A) Schematic of sarcomere structure [3]; (B) Rotated view of sarcomere showing hexagonal filament lattices [4].

Intercalated discs located at the terminal ends of cardiomyocytes are responsible for strengthening the linkage between cells as well as coordinating

contraction. Within intercalated discs, there are gap junctions that are crucial for the electric coupling of cells; in addition, there are protein complexes in the desmosomes and adherens junctions that link the contractile apparatus to the cell membrane for force transmission between cardiomyocytes. The costamere, illustrated below in Figure 1.2, is a complex protein structure that flanks the sarcomere at the Z-disk [5] and forms a molecular bridge between the sarcomere and the extracellular matrix (ECM) surrounding the cardiomyocytes [6]. Because of this linkage, costameres have been determined to play a central role in cell stability and mechanotransduction [7, 8]; the costamere has been previously shown to be the site where forces are transmitted laterally across the cell membrane [9]. Protein networks in or linked to the costamere include, but are not limited to, desmin, talin, actinin, and vinculin [5].

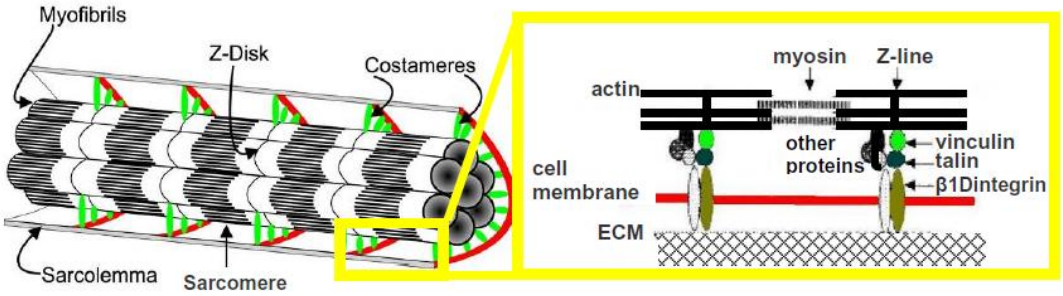

Figure 1.2: Illustration of costamere structure [1, 5].

1.2 VINCULIN

Vinculin (Vcl) is a 116-kDa membrane-associated protein found throughout the body that localizes at cell adhesion sites such as costameres, adherens junctions, and intercalated discs in cardiomyocytes [10-12]. It is a key component in the formation of focal adhesion protein complexes that link the actin cytoskeleton of

myofibrils to integrins on the cell surface in all cells [13-16]. Focal adhesions have many similarities to the costamere found in myocytes. Because of its role in costameres, Vcl has been suggested to play a significant structural role in mechanotransduction, which can result in altered cell structure and/or function [8, 17]. The presence of Vcl may allow cells to resist stresses that result from mechanical forces on the cell exterior [14]. In addition to transducing mechanical signals, Vcl could directly affect myocardial mechanical function in a direction-dependent manner due to its alignment with the costamere.

A cardiomyocyte-specific vinculin knockout (cVclKO) mouse model was created using the Cre-lox system, which allows for site specific recombination events in genomic DNA. Studies in this model revealed abnormal adherens junctions and the disbanding of intercalated discs [14]. It was observed that 49% of KO mice died prior to the age of 3 months despite having normal contractile function [14]. Those that survived beyond this age developed dilated cardiomyopathy by 16 weeks of age [14]. Previous mechanical analysis measured the effects of Vcl disruption and found significant decreases ($P<0.05$) in systolic transverse strain components *in vivo* compared with littermate controls [1]. Additionally, no change in systolic fiber strain was observed *in vivo* [1], which was consistent with preliminary observations of no change in isometric fiber tension development in isolated papillary muscles of heterozygous global cVclKO mice. Because of the importance of vinculin's structural role in costameres, Vcl ablation may affect sarcomeric structure; based on previous experimental observations, the removal of Vcl is believed to affect myocardial mechanical function in a direction-dependent manner.

1.3 LATTICE SPACING

The lattice spacing is defined as the center-to-center spacing between adjacent actin and myosin filaments; this distance can be examined by rotating the sarcomere 90^{o} about its short axis and viewing it down the axes of the filaments as seen above in Figure 1.1. Over the typical working range of sarcomere lengths, it has been shown that intact, resting myocytes maintain a constant volume; therefore, the lattice spacing must be inversely proportional to the sarcomere length. This is true for both skeletal and cardiac muscle [18, 19]. Previous studies have confirmed that while the lattice spacing of cardiomyocytes does change with sarcomere length during systole and diastole, the volume of the lattice does not appear to remain constant in the dynamic state. The change in myosin lattice spacing was consistently observed to be significantly greater during systole than diastole [18, 20]. However, it is believed that this behavior does not necessarily translate to changing lattice volume because water may be moving into the cell to maintain constant cell volume despite the alterations in lattice dimensions [20].

When sarcomere length is increased, cardiac muscle fibers are known to produce more force [21]. According to the Frank-Starling law of the heart, the activation of myofibrils by calcium increases as the length of the sarcomere increases. It is believed that this phenomenon is the result of myofilaments moving closer together (i.e. lattice spacing decreasing) as the sarcomere is stretched axially, which enhances the probability of favorable binding between actin and myosin [19]. Martin et al. (2004) concur with this assessment and attribute the increased force more

specifically to the increased probability of initial weak crossbridge binding [22]. In skeletal muscle, this binding has been shown to be required to generate force; applying this observation to cardiac muscle suggests that decreased lattice spacing could also lead to an increase in force-generating crossbridges [22].

Experiments suggest that there is an optimal lattice spacing required for force development, which is close to the *in vivo* spacing [23]. In intact skeletal muscle, isometric force decreases when the lattice spacing is decreased beyond this "equilibrium" distance by increasing sarcomere length [4]. When the lattice volume is decreased by 50% from the *in vivo* spacing, researchers observed a decrease of 80% in isometric tension [4]. In general, lattice shrinkage below the optimal dimensions in either skinned or intact muscle of both striated muscle types causes a reduction in physiological performance, which is exemplified by decreased calcium sensitivity, decreased isometric force, and increased fiber stiffness [4]. At equilibrium, all of the forces on a cell are balanced to maintain the optimal sarcomeric structure. Removal of a key structural protein could disturb the equilibrium sarcomeric structure and alter force generation. It is believed that a costameric defect, such as the deletion of Vcl, would alter myofilament lattice spacing by changing the equilibrium of stresses in the cytoskeleton.

1.4 CURRENT METHODS TO MEASURE LATTICE SPACING

Over the years, several techniques have been utilized to measure the spacing between myosin and actin filaments of striated muscle. When the myofibril was first imaged several decades ago, researchers utilized x-ray diffraction to measure this

value. Since then, this has been the most common method for measuring the lattice spacing. Low angle x-ray diffraction allows researchers to image striated muscle *in vivo* as the muscle contracts and relaxes; this data can then be analyzed to determine what effects, if any, lattice spacing has on force generation and crossbridge dynamics [4, 18]. Alternatively, researchers can utilize electron microscopy to image the filament lattice. However, this process requires careful preparation prior to imaging. Procedures such as fixation and dehydration of the sample can distort the lattice and lead to inaccurate measurements. These procedures can cause the lattice to shrink 10-20% [4, 20]. If the experiment only requires that the magnitude of the change in lattice spacing be determined at specific sarcomere lengths, either technique may be used. If neither of these techniques can be implemented during physiological experiments, several researchers have estimated changes in lattice spacing by measuring the fiber diameter throughout the experiment [4].

1.5 REGIONAL VENTRICULAR MECHANICS

Understanding cardiac pumping performance and global mechanics are essential for clinical assessment of various pathological conditions. However, it is equally important to understand the regional ventricular function. Thus far, measuring the local forces directly in the intact myocardium, even in animal models, has proven to be difficult because accurate and compatible force gauges have not been developed for intact cardiac applications. Consequently, researchers have resorted to mathematical modeling that is rooted in continuum mechanics for assessment of regional stress in the heart wall. Since they are more easily obtained, strain

measurements in the ventricular wall are typically acquired experimentally and utilized to quantify local mechanics in the myocardium [24] with methods such as speckle tracking echocardiography [25], tagged MRI [26], or implanted markers with x-ray imaging [27]. These strain measurements can help researchers understand the local mechanics and can shed light onto the mechanism for altered global function associated with cardiac pathologies. It is believed that the removal of Vcl will alter the sarcomeric structure and thus, affect the transverse systolic stress development. Studying the regional ventricular mechanics will provide insight into the mechanistic link between possible structural alterations and ventricular dysfunction associated with Vcl deletion.

1.6 MAGNETIC RESONANCE IMAGING (MRI)

A variety of clinical imaging techniques, such as x-ray computerized tomography, echocardiography and MRI, are generally employed to measure cardiac geometry and functional parameters [24]. MRI has been utilized to accurately quantify functional parameters including, but not limited to, overall geometry, stroke volume, and ejection fraction [28-31]. However, because standard MRI is unable to identify the motion of material points, the typical 2D imaging modalities will not suffice for regional strain measurements in the heart [24]. More recently, MR tagging methods have been incorporated to experimentally measure all components of the regional strain tensor *in vivo* [1, 32-34]. The premise for MR tagging is actually fairly simple. A saturation pattern is embedded in the tissue to be imaged; the initial image is then compared with the imaged pattern after the desired time period to determine

the change in shape of the underlying, patterned area [35]. Once the regional strain data has been obtained, it can be included in a mathematical model to predict regional myocardial stress distributions. This data can provide valuable insight into the effects of myocyte structural defects on regional ventricular function.

1.7 COMPUTATIONAL MODELING

Computational models based on the laws of continuum mechanics have proven to be invaluable in the study of cardiac biomechanics; they permit the user to incorporate key structural and mechanical properties of the myocardium to interpret experimental data and analyze the mechanisms behind functional changes [24, 36]. The most effective method for solving the differential equations of physiological models has proven to be the finite element method [24, 37], which divides a complex surface into a mesh comprised of numerous elements that are each prescribed the material properties of the surface.

Our laboratory's custom modeling environment (Continuity 6.4, www.continuity.ucsd.edu) allows for the simulation of physiological models by the finite element method. The computational model described in this thesis is a 3D computational model based on the geometry and fiber architecture of the mouse left ventricle (LV). The systemic circulation can be modeled using a 3-element Windkessel model, and the effects of the pericardium were neglected. Active stress is a function of time and sarcomere length while the passive stress is simulated with a strain energy function [38]. With these numerical methods, it is possible to investigate

the link between structural alterations and ventricular function as well as study the effects of various cardiac pathologies.

1.8 SCOPE OF THE THESIS

The objective of this thesis was to examine the structural and mechanical roles of Vcl in cardiac force transmission and hence regional wall function. Previous studies measured the effects of Vcl deletion on regional mechanics using MRI; therefore, we investigated the structural effects of Vcl disruption by measuring lattice spacing and sarcomere length. Using the collected data, a computational modeling approach was employed to confirm the mechanistic link between the observed structural changes and systolic force generation.

Specific Aims of the Thesis:

Aim 1: To develop electron microscopy-based methods for measuring sarcomeric lattice spacing in cardiac myocytes from tissue samples.

Lattice spacing has been classically measured using x-ray diffraction due to the effects of EM preparation on the measurements. This preliminary study will determine whether the standard EM tissue preparation and staining techniques are sufficient to image the lattice spacing of cardiomyocytes from whole-heart tissue samples. In addition, it will be determined whether a low-voltage EM (JEOL 1200EX) has sufficient resolution to measure the lattice spacing.

Aim 2: To investigate the effects of Vcl deletion on sarcomere structure.

This aim will utilize a high-voltage EM (FEI Titan) to compare the lattice spacing and sarcomere length of homozygous cardiomyocyte-specific vinculin

knockout mice (cVclKO) to that of littermate control mice with normal expression of vinculin. Images will be captured with a CCD camera on the EM; they will then be analyzed using fast Fourier transform to obtain measurements of lattice spacing and sarcomere length. At equilibrium, all of the forces on a cell are balanced to maintain the sarcomeric structure. If a key component of the cell is removed, the balance of forces will be disturbed, causing the sarcomere to establish a new equilibrium configuration. Because of vinculin's structural role in costameres, it was hypothesized that removing Vcl would alter myofilament lattice spacing by changing the equilibrium of stresses in the cytoskeleton. The sarcomere length will also be measured to ensure that the lattice spacing changes are the result of Vcl deletion and not differences in sarcomere length due to possible inconsistencies while fixing the tissue.

Aim 3: To investigate the role of sarcomeric structural changes caused by Vcl deletion in regional ventricular wall function.

Lattice spacing and sarcomere length measurements are incorporated into a computational model of regional ventricular function to illustrate the role of Vcl in regional wall mechanics. Prior experimental data using cardiac MRI tagging has shown significant decreases in the systolic sheet-normal shear and sheet strains of KO mice [1]. It is hypothesized that an increase in transverse systolic stress development may explain these results, which may be due to an increase in myofilament lattice spacing in the cVclKO hearts. It is believed that the increase in lattice spacing alters

the crossbridge binding angle of myosin heads, thereby increasing the transverse force generation.

1.9 ACKNOWLEDGEMENTS

Chapter 1, in part, is currently being prepared for submission for publication of the material. Chuang J; Janssen MS; Tangney J; Liao P; Ross RS; McCulloch AD; Omens JH. “The Role of Vinculin in Active Fiber and Sheet Mechanics.” The thesis author was the secondary investigator and author of this material.

Chapter 2

Effects of Vinculin Deletion on Sarcomere Structure

2.1 INTRODUCTION

Vinculin is a ubiquitously expressed membrane-associated protein that has been shown to localize and play key structural roles at cell adhesion sites such as costameres, adherens junctions, and intercalated discs in cardiomyocytes [10-12]. It is a key component in the formation of costameric protein complexes that link the actin cytoskeleton of myofibrils to integrins on the cell surface [13-16]. If removed, the forces regulating lattice structure will likely become unbalanced, and a new equilibrium lattice spacing would be required. Researchers believe that an optimal lattice spacing exists, which is close to the *in vivo* spacing [23]. Shrinkage or expansion of the lattice beyond the optimal dimensions causes changes in physiological performance, which are exemplified by altered calcium sensitivity, isometric force, and fiber stiffness [4].

The objective of this study was to determine whether Vcl disruption in cardiac myocytes causes alterations in sarcomeric structure. Because of the importance of vinculin's structural role and its position in costameres, it was hypothesized that removing Vcl would alter myofilament lattice spacing by changing the equilibrium of stresses in the cytoskeleton. Measurements of lattice spacing and sarcomere length

were obtained from hearts at states representative of end-diastole and end-systole using EM. Optical diffraction patterns were then generated from FFTs of the electron micrographs and analyzed to determine if the cVclKO hearts incurred any structural changes as compared to the littermate controls.

2.2 METHODS

2.2.1 Mouse Model

A cardiomyocyte-specific Vcl knockout mouse line (MLC2v-Cre/Vcl-Flox/Flox) was provided by Dr. Robert Ross's laboratory at the UCSD VA Hospital. Cre-loxP technology was utilized to excise the vinculin gene [14], creating a cardiac myocyte specific vinculin knockout (cVclKO) mouse model. Samples from the knockout mice (n = 3) were compared to Cre-negative littermate control mice (n = 3) with no Vcl excision. Female mice 5-6 weeks of age were used for this study to isolate the effects of Vcl deletion prior to the onset of heart failure. All protocols were performed according to the National Institutes of Health's *Guide for the Care and Use of Laboratory Animals* and approved by the UCSD and VA Animal Subjects Committee.

2.2.2 Intact LV Isolation, Fixation, and Embedding

All extraction and fixation procedures were performed for the author by Masahiko Hoshijima at NCMIR and were previously described by Hayashi [39]. Approximately 10-15 minutes prior to dissection, the mice were first injected intraperitoneally with 0.2 ml of 250 unit/ml heparin in PBS. The mice were then

anesthetized with a lethal dose of 21 mg/ml pentobarbital, and cervical dislocation was performed. After opening the anterior chest, the heart was extracted with the aorta by cross-cutting the aorta beyond the branching to the right carotid artery and placed in a 6 cm petri dish filled with ice cold, perfusion solution (Table 2.1). The first group of mice was arrested at end-diastole by perfusion with a modified St. Thomas No. 2 solution [40]; to simulate end-systole, the second group of mice was perfused with low-calcium Tyrode solution until flow stabilized followed by the barium-containing (2.5mM) Tyrode solution [41, 42]. The concentrations of the perfusates are shown below in Table 2.1. The ascending aorta was cannulated and manually infused with the perfusion solution to relax the heart before connecting the needle to a Langendorff perfusion apparatus with a hydraulic pressure of 90 cm H_2O for 3-5 minutes. The hearts were then perfusion fixed with 2% paraformaldehyde and 2.5% glutaraldehyde in 0.15M sodium cacodylate buffer (pH 7.4) for approximately 10-15 minutes before being removed from the perfusion apparatus. The mid-LV of the diastolic hearts was isolated via transverse sectioning using a sharp blade while tissue from the barium-contracted hearts was isolated via sectioning along the sagittal plane. Due to the transmural fiber angle variability in the heart, the change in sectioning direction was implemented to increase the ease with which the lattice was imaged.

Following the fixation, the tissue was put in a Petri dish with ice-cold 0.1M sodium cacodylate buffer. Postfixing was completed in ice-cold 2% osmium tetroxide and 0.8% potassium ferrocyanide in 0.1M sodium cacodylate buffer on ice overnight. The next morning, the tissue slices were rinsed in double-distilled water (DDW) 3

times for 3 minutes before being placed in ice-cold 2% uranyl acetate in DDW for 1-2 hours on ice to stain and stabilize the tissue. Tissue was then dehydrated in a graded series of ice-cold ethanol (EtOH) solutions (20, 50, 70, 90% ethanol in DDW) for 10 minutes followed by dehydration in 100% EtOH 3 times for 10 minutes at room temperature. After dehydration was complete, the tissue was infiltrated in well-mixed solution of 67% EtOH / 33% Durcupan ACM resin for at least 4 hours, followed by a 50:50 mixture and 33% EtOH / 67% Durcupan solution for 4 hours each. The tissue was further embedded in approximately 2 ml of 100% Durcupan ACM for at least 8 hours 3 times while being agitated on a rotator. Finally, the embedded tissue was placed in a vacuum oven to polymerize at 60-80^{o}C for 48 hours.

Table 2.1: Chemical composition of perfusion solutions utilized during tissue extraction and fixation processes. All solutions have been adjusted to a pH of 7.5, and the listed compositions have units of mM.

Solution Name	**NaCl**	**KCl**	**$MgCl_2$**	**H_2O**	**$NaHCO_3$**	**HEPES**	**Gluc.**	**$CaCl_2$**	**$BaCl_2$**
Low-Ca Tyrode	137	2.7	1	2.6	4	10	5.5	0.078	N/A
St. Thomas No. 2	110	16	16	N/A	10	10	5.5	1.2	N/A
Ba^{2+}-Tyrode	137	2.7	1	2.6	4	10	5.5	0.078	2.5

2.2.3 EM Sample Preparations

2.2.3-A Block Trimming:

A small piece of LV free wall was trimmed from the embedded specimen, adhered to a cylindrical plastic block using cyanoacrylate glue, and allowed to dry overnight to ensure adhesion; two blocks were prepared for each mouse. After securing the block in the specimen holder assembly of a Reichart-Jung Ultracut E ultramicrotome, a single-edge razor blade was used to trim the top surface of the block

and expose a 1 mm by 1 mm square region of interest [43]. The exposed surface was raised a minimum of 0.5 mm above the block to avoid contact in subsequent steps. The specimen holder assembly was then returned to the sectioning arm for smooth trimming, and the return speed switch was set to position 1. A glass knife was inserted into the knife carrier assembly before adjusting the clearance angle calibration control to 5^o and the horizontal knife alignment to 25^o. The end point on the control lever was specified slightly below the cutting edge of the knife. The exposed surface of the block was then trimmed into a trapezoid with sides at 10^o [44]; this shape helped relieve stress on the glass knife and prevent it from cracking during sectioning.

Once the trapezoid shape was completed, the block was rotated such that the short edge was on the bottom, and the horizontal knife alignment was returned to 0^o. The glass knife was advanced manually with the hand wheel until it was aligned with the surface of the block. Using the calibrated manual advance feed knob to move the block forward at 0.5 μm increments, the surface was trimmed to remove excess plastic covering the top of the tissue and smooth the sectioning surface.

2.2.3-B Tissue Sectioning:

Before mounting the glass sectioning knife, the interior of the boat was rinsed with DDW to remove any collected dust. The knife was then secured in the knife carrier assembly, and the end point of the drive system was specified below the top edge of the knife as before. The return speed switch was changed to position 2 for sectioning with a glass knife, and the cutting speed was adjusted to 0.6 mm/s. The boat was filled completely with water; using a syringe, water was removed from the

boat until the water surface appeared silver through the stereomicroscope. With the magnification of the microscope set to 1x, the knife was moved forward until a shadow appeared on the surface of the block. Using the shadow as a guide, the horizontal knife alignment was adjusted until the shadow thickness was uniform across the width of the block; then, the swivel knob on the specimen holder assembly was adjusted until the shadow thickness was consistent while moving the block up and down. The feed range was set to 0.25 μm, and the control level pushed down to begin sectioning.

The interference color [43, 45] and its uniformity across the sections were used as determinants for acceptable sections. It was decided that blue (190-240 nm) and purple (150-190 nm) sections would be used to ensure that the sections were not too thick for imaging. Using self-closing forceps, a 200 mesh, copper grid was passed through the flame of a lighter and rinsed in DDW to remove copper precipitates. The "pull up method" was utilized to remove sections from the boat [44]. Grids were dabbed on filter paper to remove excess water before being stored in a grid box. A minimum of 10 quality sections were taken from each block.

2.2.3-C Section Staining:

To enhance the contrast of biological structures in EM images, sections were stained with lead citrate and a 1% (w/v) aqueous solution of uranyl acetate (UA); lead citrate stains proteins and glycogen granules while UA stains nucleic acids. A vial of 1% UA was created using equal parts by volume of 2% UA and DDW. A vial of 0.01N-sodium hydroxide (NaOH) was created with 9.9 ml DDW and 0.1 ml 1N-

NaOH. A schematic of the staining setup is shown below in Figure 2.1. The fluid in each weighing dish was filtered through a 0.22 μm filter unit before being added. Grids were carefully laid face down on the surface of each dish and moved between dishes using a platinum loop. After going through all stages, the grids were blotted with filter paper and allowed to air dry for 5-10 minutes.

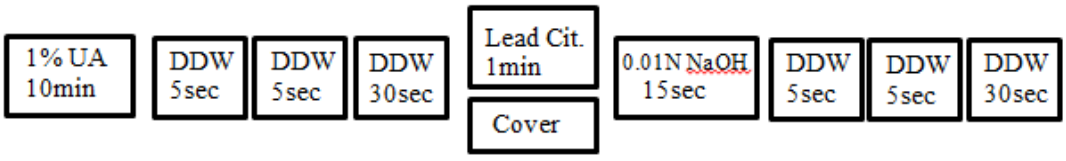

Figure 2.1: Schematic of weighing dishes used during section staining as well as the times required in each dish; the lead citrate requires a cover dish at all times to prevent precipitation from carbon dioxide.

2.2.3-D Carbon Coating:

Following staining, sections were coated with carbon using Cressington's High Vacuum Turbo Carbon Coater to increase the stability of the specimen in the electron beam. Four grids were placed on the rubber block and secured inside the vacuum chamber. The gauge and leak switches were put in the on and off positions, respectively. Once on, the chamber was pumped down to 10^{-4} mbar before coating the grids with carbon for 15 seconds. When complete, the grids were turned over and the process repeated for the other side.

2.2.4 Imaging Protocol

All electron microscopy images were taken on the FEI Titan, which is equipped with a Gatan 4k x 4k Ultrascan 4000 camera, and the FEI Spirit, which is equipped with a Gatan 2k x 2k CCD camera; the latter was only used on two

occasions when the Titan was inoperable. Previously saved alignments were loaded, and the eucentricity was adjusted to ensure proper alignment when tilting the stage. When a region of interest was located, the image was focused, and the stage tilt was adjusted manually such that the tissue was oriented perpendicularly to the camera. The SerialEM interface was utilized to record single images, montages, and tilt series; during a tilt series, the software predicts the position of the sample based on its position in previous tilts [46]. Tilt series images were obtained from -30^{o} to $+30^{o}$ at 2^{o} increments. Single images of the lattice were acquired at x37,000-47,000 magnification while those of sarcomere length were taken at x3,800-5,000 magnification.

2.2.5 Image Analysis and Measurements

2.2.5-A Lattice Spacing Images:

Images of the lattice were imported into the National Institutes of Health's image processing and analysis software, ImageJ. To ensure the accuracy of the measurements, the analyzed lattice must be perpendicular to the camera; these regions are chosen based on the regularity of the live Fourier transform image on the electron microscope as well as the circularity of the filaments. A square region (2^{n} x 2^{n} pixels) of lattice was selected and cropped from the original image. This region was transformed by fast Fourier transformation (FFT) into the spatial frequency domain. The brightness and contrast were adjusted to better visualize the intensity spots before being filled by adjusting the threshold. Using the tracing utility, the center of mass coordinates were obtained, which were then utilized in conjunction with the

Pythagorean theorem to calculate the distance between intensity spots. Because the transformed image represents reciprocal space, the distance to the first-order diffraction pattern corresponded to the center-to-center distance between myosin filaments while the second-order pattern related to the distance between actin and myosin. Equation 2.1 was utilized in conjunction with the pixel sizes of the images [47] to calculate the lattice spacing from the transformed measurement.

$$LS(nm) = \frac{distance\ in\ FFT * pixel\ size}{total\ image\ width} \qquad (2.1)$$

2.2.5-B Sarcomere Images:

Analysis of sarcomere images with FFT was performed as described in section 2.2.5-A. Often times, higher order diffraction patterns had to be utilized to obtain the sarcomere length due to the proximity of the first-order to the FFT center. Sarcomere length measurements were verified manually by averaging the distance of 3-4 sarcomeres in one fiber. Unlike with the lattice spacing analysis, the entire image was often used when calculating sarcomere length.

2.2.6 Statistical Analysis

All data shown is expressed as mean values ± standard deviations, and *n* represents the total number of samples. A two-tailed, unpaired Student's *t*-test was utilized to compare the mean lattice spacing and sarcomere length measurements between cVclKO and Cre-negative control mice. P-values < 0.05 were considered statistically significant.

2.3 RESULTS

Lattice spacing and sarcomere length were measured from optical diffraction patterns generated from FFTs of electron micrographs. Figure 2.2 shows representative EM images of the lattice and sarcomere as well as their respective optical diffraction patterns generated in ImageJ.

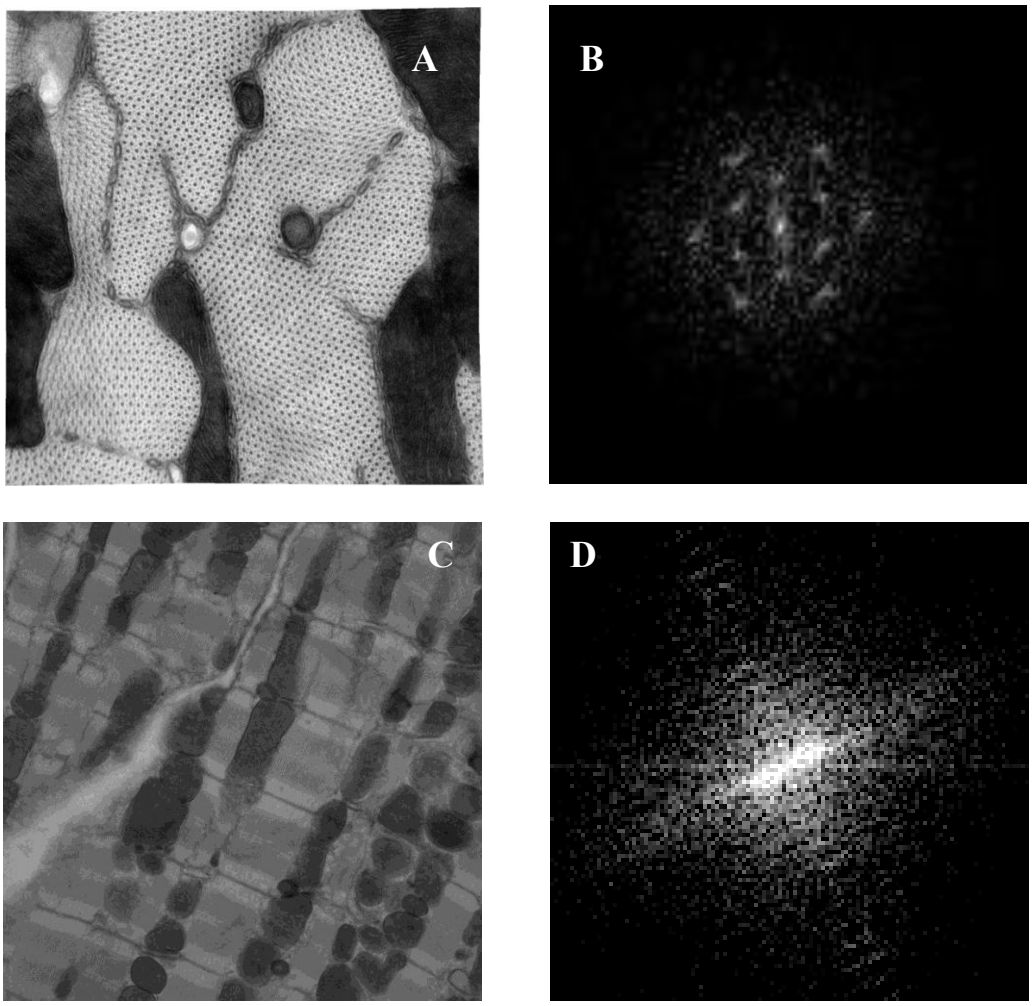

Figure 2.2: Images and data obtained during sarcomere image analysis. (A) 3 x 3 image montage of cardiac myofilament lattice captured on FEI Titan at x47,000 magnification. Each image has dimensions of 4,096 x 4,096 pixels, and the pixel size is 0.19 nm; (B) Optical diffraction pattern of 1 image from the montage generated in ImageJ; (C) Image showing sarcomere length captured on FEI Titan at x3,800 magnification and pixel size of 2.35nm; (D) Optical diffraction pattern of sarcomeres generated in ImageJ.

Table 2.2 compares the average lattice spacings and sarcomere lengths from the KO end-diastolic hearts to those of the control hearts. Table 2.3 compares these measurements in the barium-contracted hearts. Because the sarcomere length varies from mouse to mouse within an experimental group, the myofilament lattice spacing was normalized to the sarcomere length to evaluate the effects of Vcl disruption. The normalized spacing of the end-diastolic hearts was significantly higher ($P<0.05$) for the cVclKO as compared to the Cre-negative controls. A similar trend was observed for the barium-contracted hearts, but no statistically significant difference was found.

Table 2.2: Comparison of average SL and lattice spacing (LS) measurements for cVclKO (n=3) and control (n=3) hearts arrested at end-diastole with calcium-free Tyrode solution. The normalized lattice spacing is unitless.

cVclKO					Control			
ID #	**SL (um)**	**LS (nm)**	**LS/SL**		**ID #**	**SL (um)**	**LS (nm)**	**LS/SL**
5506	1.77	19.45	0.011		5507	1.90	17.66	0.009
5511	1.69	20.44	0.012		5510	1.87	19.05	0.010
5517	1.76	19.15	0.011		5516	2.19	19.56	0.009

Table 2.3: Comparison of average SL and lattice spacing (LS) measurements for cVclKO (n=3) and control (n=3) hearts simulated at end-systole using barium-contracture. The normalized lattice spacing is unitless.

cVclKO					Control			
ID #	**SL (um)**	**LS (nm)**	**LS/SL**		**ID #**	**SL (um)**	**LS (nm)**	**LS/SL**
8214	1.39	21.89	0.016		8209	1.42	18.70	0.013
8215	1.53	21.01	0.014		8210	1.43	19.93	0.014
8216	1.37	20.99	0.015		8212	1.64	19.82	0.012

Figure 2.3 below illustrates the relationship between the normalized lattice spacing and contraction state for the two experimental groups. The two curves have the same slope but different y-intercepts. On average, it seems that at a given SL the

KO mice have larger lattice spacings than their control counterparts. Two-way non-repeated ANOVA was used to determine the statistical significance of the average normalized lattice spacing of the two genotypes at each contraction state; the average KO lattice spacing was significantly higher ($P<0.05$) than the control spacing, and the spacing in the barium-contracted hearts was significantly higher ($P<0.01$) than that in the end-diastolic hearts. Also, the interaction between the two curves was determined to not be significant, which was expected because the two curves are parallel. To confirm whether this held true for individual mice, the sarcomeric volume ($V = \pi * SL * LS^2$) for each KO mouse was calculated; then, assuming the sarcomeric volume was conserved, a new lattice spacing was calculated based on the SL of each control mouse. This analysis can be found in Appendix A and demonstrated that the increased KO lattice spacing was the result of structural changes, not the measured differences in SL.

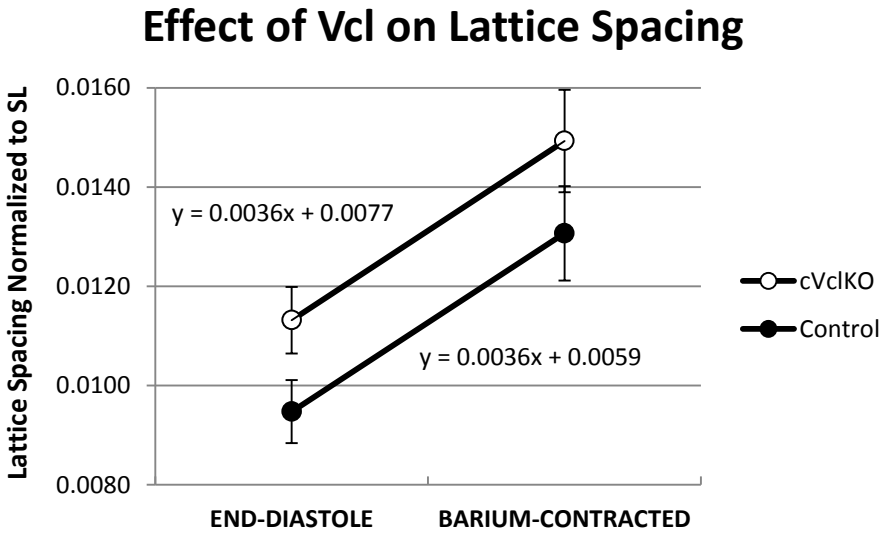

Figure 2.3: Effect of Vcl deletion on actin-myosin filament spacing normalized to sarcomere length in mouse hearts arrested in end-diastolic and barium-contracted states.

Finally, the normalized center-to-center spacing between myosin filaments was also calculated. As before, it was found to be significantly higher in the cVclKO end-diastolic hearts ($P<0.05$) while no significant difference was found in the barium-contracted hearts. The average normalized spacing between myosin filaments was determined to be 0.0263±0.0021 in barium-contracted cVclKO hearts compared with 0.0221±0.0024 in Cre-negative controls. In hearts fixed at end-diastole, this spacing averaged 0.0193±0.0013 in cVclKO *vs.* 0.0156±0.0013 in the control mice.

2.4 DISCUSSION

In this study, we examined the effect of vinculin deletion on sarcomeric structure in murine hearts. cVclKO mice were studied at 5-6 weeks of age before the onset of cardiac failure associated with this genotype [13, 14]. Previously published x-ray diffraction results for vertebrate heart muscle [48] yielded a center-to-center distance between myosin filaments of 42 nm at a sarcomere length of 2.2 μm. Using the measured normalized spacing values and a sarcomere length of 2.2 μm, an average center-to-center myosin spacing of 34 nm was calculated, which is consistent with the previously reported amount of lattice shrinkage (10-20%) due to EM sample preparation methods [4]. On average, the myofilament lattice spacing of the cVclKO hearts was significantly higher ($P<0.05$) than the Cre-negative control hearts in the end-diastolic state; while a similar trend was observed for the barium-contracted hearts, there was no significant difference between the two experimental groups.

Sarcomeric structure is closely linked to mechanical function. Researchers believe that an optimal lattice spacing exists, which is close to the *in vivo* spacing [23].

Shrinkage or expansion of the lattice beyond the optimal dimensions causes changes in physiological performance, which is exemplified by altered calcium sensitivity, isometric force, and fiber stiffness [4]. Studies have shown that when sarcomere volume is decreased by 50%, isometric tension decreases by approximately 80% [4]. Based on these observations, the increased lattice spacing and sarcomere volume observed in cVclKO mice could significantly alter the crossbridge orientation, thus impacting force generation.

Assuming the location of the actin binding site is unchanged between the two genotypes, an increase in lattice spacing would increase the length of the S2 segment of the crossbridge. As a result, one would expect the angle between the S2 segment of the head and the body of the myosin filament to also increase. The change in angle would cause the radial component of the crossbridge force to increase and the axial component to decrease. However, previously reported data have demonstrated no changes in systolic fiber strain of cVclKO hearts *in vivo* [1]. Thus, there must be a compensative mechanism in the KO mice that allows for the simultaneous existence of these seemingly contradictory observations. In cVclKOs, there may be other compensatory structural changes that counteract the weakening of the costamere; these changes may increase the stiffness in the radial direction and explain how the fiber strain could remain unchanged.

There were several limitations to the structural measurements. Ideally, these measurements would be obtained using x-ray diffraction to avoid the lattice shrinkage described previously. In addition, it has been previously shown that the sarcomere length varies transmurally in the left ventricle [49]. For this reason, the lattice spacing

and sarcomere length measurements would ideally be taken at the same transmural location. Unfortunately, the grids utilized in sectioning interfered with the FEI Titan's ability to image at an angle, and the dimensions of the sections were not appropriate to image in this manner; a cube of tissue would have been more desirable. While it is assumed that a similar variability exists in the control mice, the transmural variation for the cVclKO mice is unknown. For these reasons, the EM measurements may not be as accurate as possible.

Regardless, the EM studies revealed interesting changes in sarcomeric structure in cVclKO hearts. The KO mice exhibited increased myofilament lattice spacing as compared to the control mice with normal Vcl expression; based on this result, it is believed that a compressive cytoskeletal pre-stress is acting tangentially to Z-disk, which is partially released by the ablation of Vcl causing the lattice to expand. The increase in KO myofilament lattice spacing as compared to the littermate controls could affect crossbridge force generation. Previous studies have shown that Vcl deletion does in fact alter systolic force generation. A possible mechanism for these observations has been proposed, but it is unknown at this time whether the structural changes in the KO hearts are the primary cause for the mechanical alterations associated with Vcl disruption.

2.5 ACKNOWLEDGEMENTS

Chapter 2, in part, is currently being prepared for submission for publication of the material. Chuang J; Janssen MS; Tangney J; Liao P; Ross RS; McCulloch AD;

Omens JH. “The Role of Vinculin in Active Fiber and Sheet Mechanics.” The thesis author was the secondary investigator and author of this material.

Chapter 3

Mechanistic Link Between Defective Vinculin and Ventricular Dysfunction

3.1 INTRODUCTION

MRI has been utilized to accurately quantify cardiac functional parameters [28-31] and has proven to be a useful clinical imaging technique for murine hearts. Because standard MRI is unable to identify the motion of material points, MR tagging methods have been incorporated to experimentally measure the components of the regional strain tensor *in vivo* [1, 32-34]. Experimental strain measurements can then be utilized in conjunction with computational models based on the laws of continuum mechanics to quantify internal stresses at the level of the myocardium. This numerical method can be utilized to investigate the link between structural alterations and ventricular function. The resulting data can provide valuable insight into the effects of myocyte structural defects associated with Vcl ablation on regional mechanics.

The previous chapter described the structural effects of Vcl deletion from cardiac myocytes. Research has shown that changes in lattice structure beyond the equilibrium spacing negatively affect the physiological performance of the cells [4]. Previous experiments found this to be true for Vcl disruption and demonstrated that deletion of Vcl from cardiomyocytes results in altered ventricular mechanical function [1]. MR tagging revealed that Vcl disruption causes significant decreases in systolic

sheet-normal shear strain (P<0.05) and systolic sheet strain (P<0.05) *in vivo* as compared with littermate controls [1] (Figure 3.1). In addition, no change in systolic fiber strain was observed *in vivo* [1], which was consistent with preliminary observations of no change in isometric fiber tension development in isolated papillary muscles in heterozygous global cVclKO mice.

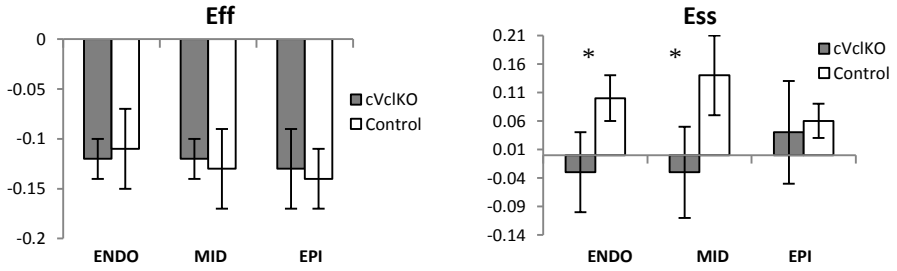

Figure 3.1: Effects of Vcl deletion on the (A) fiber and (B) sheet strains measured experimentally in mice with MR tagging [1].

The objective of this aim was to determine whether the measured changes in sarcomeric structure are directly responsible for the observed alterations in ventricular function. We hypothesized that the variations in systolic strains could be attributed to an increase in the myofilament lattice spacing of the KO mice, which in turn changes the crossbridge binding angle of the myosin heads and stiffness of the crossbridge. A geometrical analysis [50] was used to determine how changing the lattice geometry affects the binding angles and the distribution of forces at the level of the crossbridge. Additionally, the effects of fiber angle dispersion about the mean were taken into account to quantify the force distribution for a region of tissue. A finite element model was then utilized in conjunction with the calculated distribution of forces to verify the mechanistic link between Vcl disruption and ventricular dysfunction.

3.2 METHODS

3.2.1 Effect of Geometry on Stress Scaling Factors

A simplified mechanical model was used to determine the crossbridge stiffness based on the measured lattice spacing and crossbridge orientation. Components of the active stress tensor in the radial (T_{rr}) and cross-fiber directions (T_{cc}) were added as constant fractions of fiber stress (T_{ff}): $T_{rr} = K_r * T_{ff}$ and $T_{cc} = K_c * T_{cc}$. These fractions were calculated for a single myofiber using a modified version of Schoenberg's analysis [50], which examines the effects of geometrical factors on force development. Figure 3.2 shows simplified top-down and end-on 2D views of the actin-myosin crossbridge.

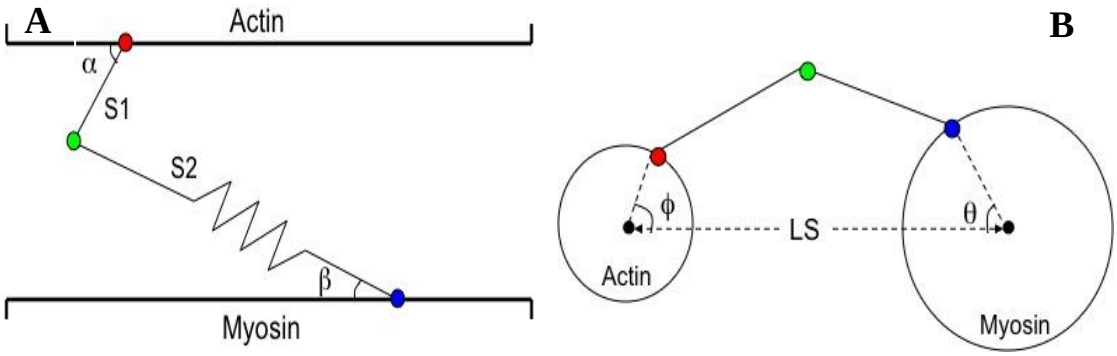

Figure 3.2: (A) Simplified 2D schematic of actin-myosin crossbridge with S2 represented as an extensible spring where the red dot = actin binding site, green dot = S1-S2 junction, and blue dot = S2 origin; (B) End-on view illustrating the rotation of the crossbridge out of plane ε, where the colored dots are projections of the aforementioned points.

Table 3.1: Description and values for the constants used in the geometrical analysis.

Variable	Description	Value	Units	Source
k	S2 spring constant	2	pN/nm	[51]
x0	S2 spring resting length	20	nm	[51]
S2	S2 length	40	nm	[50]
S1	S1 Length	16	nm	[50]
α	Axial angle of attachment	45	deg	[50, 52, 53]
ϕ	Azimuthal location of actin binding	60	deg	[50]

Table 3.1 (Continued): Description and values for the constants used in the geometrical analysis.

Variable	Description	Value	Units	Source
θ	Azimuthal location of S2 origin	60	deg	[50]
γ	Azimuthal location of the crossbridge	45	deg	[50]
R_m	Radius of myosin	5.5	nm	[54]
R_a	Radius of actin	3	nm	[54]

Table 3.1 details the values used for each of the geometrical parameters in the sarcomere stress analysis [50]. The crossbridge was permitted to rotate out of plane ε as shown in the end-on view; plane ε is defined by the S2 origin (blue dot) and actin binding site (red dot) and is parallel to the filament axes. The angle of rotation (δ) was a function of a few geometrical angles and the azimuthal location of the crossbridge (γ), which was assumed to be 45^o. The S2 length was represented by an extensional spring and allowed to change length with the sarcomeric geometry while S1 was modeled as a rigid body. In addition, the axial tilt angle of the attachment site (α) was assumed to be constant at 45^o because this has been shown to be the preferred angle of attachment [50, 52, 53]. These calculations were implemented into a MATLAB script that can be found in Appendix B.

3.2.2 Effect of Fiber Dispersion on Stress Scaling Factors

The result of the stress analysis at the level of the crossbridge is a stress distribution for a single fiber. If all of the fibers in the myocardium were oriented along the same direction, the stress tensors would all be the same; however, this is not the case physiologically as a dispersion of fiber angles about the mean exists for any given region. Therefore, the individual stress distributions associated with each local fiber direction must be accounted for. The fiber angle dispersion can be described by

two planar angles (λ and μ), which correspond to rotations about the radial and cross-fiber axes, respectively. One of these angles (λ) is shown in Figure 3.3 below. The higher order sheet structure was not accounted for in this analysis so the dispersion of the sheets themselves was neglected.

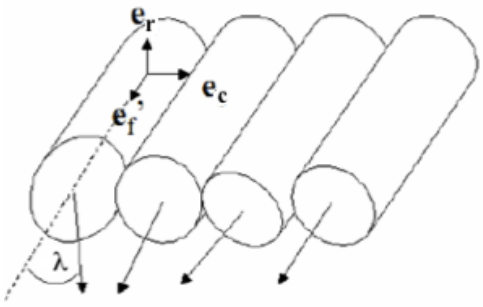

Figure 3.3: Schematic illustrating one planar angle describing the fiber angle dispersion where e_f' corresponds to the mean fiber axis of the region; λ is measured about the radial axis and is defined as the angle between a single myocyte's fiber axis and the mean fiber axis [55]. The second planar angle (μ), not shown here, is measured about the cross-fiber axis.

The effect of the fiber variation about the radial axis (λ) is governed by Eqn. 3.1. Equation 3.2 details the rotation matrix ($\mathbf{R}_\lambda$) that rotates the fiber stress tensor ($\mathbf{T}_{\text{fiber}}$) about the radial axis through a given fiber angle to the local fiber coordinate axis. If the fiber stress tensor is defined as shown below and the material is assumed to be transversely isotropic, then the transverse stress ratio calculated in the previous section is equal to the K_c and K_r factors in the fiber stress tensor.

$$\boldsymbol{T}^* = \int_{-\pi/2}^{\pi/2} \boldsymbol{R}_\lambda \cdot \boldsymbol{T}_{fiber} \cdot \boldsymbol{R}_\lambda^T \cdot f(\lambda) \cdot d\lambda \qquad [3.1]$$

$$\boldsymbol{T}_{fiber} = \begin{bmatrix} T_{ff} & 0 & 0 \\ 0 & K_c \cdot T_{ff} & 0 \\ 0 & 0 & K_r \cdot T_{ff} \end{bmatrix} \textit{ with respect to: } \{\boldsymbol{e}_f, \boldsymbol{e}_c, \boldsymbol{e}_r\}$$

$$\boldsymbol{R}_{\lambda} = \begin{bmatrix} \cos(\lambda) & \sin(\lambda) & 0 \\ -\sin(\lambda) & \cos(\lambda) & 0 \\ 0 & 0 & 1 \end{bmatrix} \textit{ with respect to: } \{\boldsymbol{e}_f, \boldsymbol{e}_c, \boldsymbol{e}_r\} \quad [3.2]$$

where $\mathbf{e}_f$ represents the fiber direction, $\mathbf{e}_r$ represents the radial direction, $\mathbf{e}_c$ represents the cross-fiber direction ($\mathbf{e}_c = \mathbf{e}_r \times \mathbf{e}_f$), and $f(\lambda)$ is the probability density distribution function for λ. Additionally, the effect of the second variation (μ) is described by Eqn. 3.3. Equation 3.4 details the rotation matrix ($\mathbf{R}_{\mu}$) that rotates the stress tensor about the cross-fiber axis.

$$\boldsymbol{T} = \int_{-\pi/2}^{\pi/2} \boldsymbol{R}_{\mu} \cdot \boldsymbol{T}^{*} \cdot \boldsymbol{R}_{\mu}^{T} \cdot f(\mu) \cdot d\mu \quad [3.3]$$

$$\boldsymbol{R}_{\lambda} = \begin{bmatrix} \cos(\mu) & 0 & \sin(\mu) \\ 0 & 1 & 0 \\ -\sin(\mu) & 0 & \cos(\mu) \end{bmatrix} \textit{ with respect to: } \{\boldsymbol{e}_f, \boldsymbol{e}_c, \boldsymbol{e}_r\} \quad [3.4]$$

Because the exact fiber distributions were unknown, $f(\lambda)$ and $f(\mu)$ were assumed to be sufficiently described using von Mises distributions centered about the mean orientations [56, 57] with angular deviations of 12^{o} [55, 57]:

$$f(\lambda) = \frac{\exp(\kappa \cos 2\lambda)}{2\pi I_0(\kappa)} \quad [3.5]$$

where the mean orientation is 0^{o}, κ is a concentration parameter, and I_0 is the modified Bessel function of order 0. The concentration parameter can have any value between 0 and ∞ with smaller values being associated with larger dispersions, and vice versa. The relationship between the concentration parameter and the angular dispersion (AD) [56, 57] is given by:

$$AD = \frac{I_0(\kappa)}{\kappa \cdot I_1(\kappa)} \quad [3.6]$$

where I_1 is the modified Bessel function of order 1, and the concentration parameter (κ) corresponding to an angular dispersion of 12^o is 5.3. All integrals described above were numerically integrated using a MATLAB script, which can be found in Appendix C.

3.2.3 Active Contraction Simulations

To investigate the role of sarcomeric structural alterations due to Vcl disruption on systolic wall mechanics, a simplified model of a mouse LV was implemented with the laboratory's FEM software (Continuity 6.4). The LV was approximated using a truncated ellipse of revolution with the focal length of the prolate spheroid set to 3.75 mm [30]. The axisymmetric geometry was divided into 3 sections longitudinally and 4 sections radially as shown in Figure 3.4.

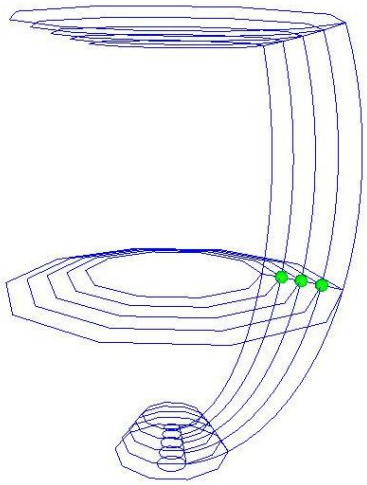

Figure 3.4: LV geometry implemented in Continuity for active contraction simulations illustrating the approximate locations of the Gauss points of interest.

The passive mechanics of the myocardium were modeled as a slightly compressible, transversely isotropic material with respect to the fiber and transverse-fiber directions [58]. Fiber angles measured at the equator in the control mice [1]

were incorporated throughout the mesh. At zero pressure, the unloaded geometry had a cavity volume of 30 μl. The unloaded geometry was first inflated using a linear increase in pressure to an end-diastolic pressure of 1.34 kPa. These nodal coordinates were saved for later use when calculating strains. The LV was then simulated to contract against a three-element Windkessel circulation model with the following parameters: initial aortic pressure = 10.66 kPa, arterial compliance = 12,000, aortic impedance = 0.012, and peripheral resistance = 0.14. The active tension model was a time-varying elastance model in which active tension is only a function of sarcomere length and time [59].

The end-systolic time point was determined by the closure of the aortic valve, which occurs when the aortic pressure exceeds the left ventricular pressure. The nodes at this time point were input into Continuity. The previously saved end-diastolic nodes were loaded as well so that the end-systolic strains were calculated with respect to the end-diastolic state instead of the zero-pressure state. Finally, the strains were output through Continuity at the 3 preselected Gauss points near the three nodes shown in Figure 3.4 corresponding to the endocardium, mid-wall, and epicardium.

3.3 RESULTS

3.3.1 Effect of Geometry & Fiber Dispersion on Stress Scaling Factors

The ratio (K_r) of radial force to fiber force was calculated for an individual fiber using the myofilament lattice spacings measured with EM and the aforementioned geometrical analysis. This ratio was determined to be 0.0991 for the

control hearts and 0.1651 for the KO hearts. Using the spring constant (k) and resting length (x0) mentioned above in Table 3.1, the force in the S2 segment could be resolved. These values in conjunction with the sarcomere stress analysis [50, 60] allow for the calculation of the individual components of the crossbridge force. The radial and fiber components of the total force were estimated to be 3.95 pN and 39.8 pN, respectively, for the control mice; in the KO mice, these components were approximately 6.63 pN and 40.1 pN, respectively. Therefore, the increase in K_r can be attributed mostly to an increase in the radial component of the force.

The transverse components of the single fiber stress tensor were defined as constant fractions of the fiber stress, where the fractions (K_c and K_r) were equal to stress ratio calculated using the sarcomere stress analysis [50, 60]. The effects of fiber dispersion were then taken into account to determine the stress tensor for a region of tissue. Angular dispersions of 12^o about the radial and cross-fiber axes increased the K_c value to 0.159 for the control and 0.227 for the KO; because the tissue is assumed to be transversely isotropic, the K_r value is increased by the same amount. When compared to the ratios from the geometric analysis, this is an increase of 60% and 38% for the control and KO, respectively. Stress ratios of this magnitude most likely represent the maximum values because it is unlikely that the standard deviation of the fiber dispersions (λ and μ) would be as large as the 12^o described previously [55].

3.3.2 Active Contraction Simulations

A simplified finite element model of the mouse LV was created to investigate the mechanistic link between the structural alterations and systolic wall mechanics

associated with Vcl deletion. A baseline control model for the Cre-negative mice with normal expression of Vcl was generated using the calculated distribution of forces: $K_r = K_c = 0.159$. The end-systolic strain results are shown in Figure 3.5 alongside the experimental MR tagging results [1] for the three normal directions. To simulate an increase in transverse stiffness associated with the increased lattice spacing of the cVclKO, K_r and K_c were increased to 0.227. This change reflected the calculated change in the force distribution based on the lattice geometry and fiber angle dispersion. The fiber strain and cross-fiber strain of the control model were determined to be negative while the radial strain was positive, all of which coincide with the experimental observations. A comparison of the two genotypes revealed that the effects of Vcl deletion are qualitatively similar to those observed in the cVclKO MR tagging experiments. As shown in Figure 3.5, fiber strain was not altered significantly from the baseline model as predicted by the geometrical analysis. Conversely, the radial strain decreased with the increase in the transverse stress ratio. While a similar trend was observed in the cross-fiber direction with the strain increasing slightly in the KO, the magnitude of the change was much smaller than that observed experimentally.

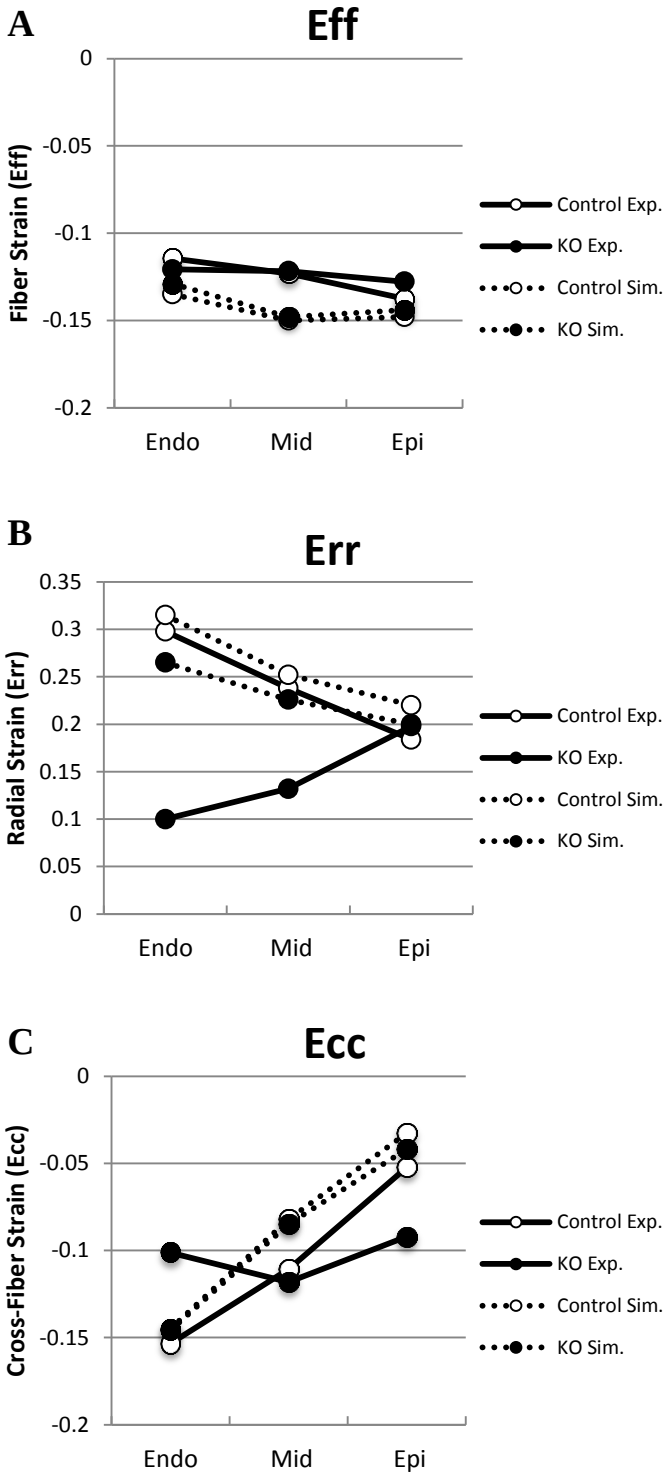

Figure 3.5: Comparison of the effects of Vcl deletion on the (A) fiber, (B) radial, and (C) cross-fiber strains predicted by the finite element model to those measured experimentally [1] in mice with MR tagging.

3.4 DISCUSSION

A simplified mechanical analysis of the crossbridge demonstrated that the removal of Vcl from cardiac myocytes causes significant changes to the crossbridge orientation. The increased myofilament lattice spacing of the KO increases the angle of the crossbridge with the myosin filament as well as its rotation out of plane ε. The increased angle of the KO model resulted in an increase in the ratio of transverse to fiber forces (K_r and K_c) generated by the crossbridge. Because it was assumed that the actin binding site remained unchanged, the change in angle also increased the length of the S2 segment of myosin, which was modeled as an extensible spring. Resolution of the crossbridge force components showed that the increased KO ratio was attributed to an increase in the transverse component. The results of this analysis confirmed the hypothesis that an increase in the transverse stiffness of the cVclKO as compared to the control compensates for the decrease in fiber strain that would be expected from an increase in crossbridge angle (i.e. β in Figure 3.2). These outcomes are consistent with experimental data [1] demonstrating that Vcl removal does not have a drastic effect on the strain in the fiber direction due to the fact that its removal does not affect the cardiomyocytes' ability to shorten at the examined age.

In addition to examining the effect of lattice geometry on a single fiber's force distribution, the effect of fiber dispersion was also taken into account to determine the force distribution for a region of tissue. Because no fiber angle measurements were obtained in the present study, the dispersions were assumed to be sufficiently described by von Mises distributions with angular deviations of 12^o. The fiber

dispersion is unlikely to be this high [55] so the use of this value represents the maximum effects of fiber dispersion on force distribution. Accounting for the fiber dispersion exacerbated the difference in the transverse to fiber stress ratio between the KO and control. Closer inspection of the regional stress tensor illustrated that the fiber dispersion caused a redistribution of part of the fiber stress to the cross-fiber direction. Because the tissue was modeled as a transversely isotropic material, the fiber stress is equally redistributed to the radial direction. This result offers further credence to the notion of an increase in transverse crossbridge stiffness when Vcl is removed; if the altered lattice spacing does not affect the crossbridge stiffness, the redistribution of forces in the aforementioned geometrical analysis would be similar to that shown here with the fiber stress decreasing instead of remaining constant.

The regional stress tensor was input into a finite element model to determine whether the observed changes in lattice spacing were directly responsible for the observed alterations in regional ventricular mechanics. To simplify the model, the higher order sheet structure of the heart was not considered. Because of the fibrous architecture of the myocardium, the LV was modeled as a transversely isotropic material [24, 61]. K_c and K_r were increased to simulate the increased transverse crossbridge stiffness in the cVclKO. It is believed that an additional structural change may compensate for the removal of Vcl from the costamere, but the exact cause of the increased stiffness is not known at this time.

Based on previously reported fiber orientations, the cardiac strains measured in the cVclKO MR tagging experiments [1] were transformed into the fiber/cross-fiber coordinate system. These measured strain values could then be accurately compared

to the results of the finite element model, which neglected the effects of sheet structure. In the control simulation, E_{ff} and E_{cc} were negative, indicating fiber and cross-fiber shortening, respectively; E_{rr} was positive, indicating radial thickening. The direction and transmural trends are consistent with other animal studies. The simulation fiber strains exhibit a relatively uniform transmural variation, which is consistent with fiber strain values in dog studies [61, 62] and the MR tagging experiments [1]. Additionally, radial and cross-fiber strains have been previously shown to have substantial transmural gradients and be largest at the endocardium [61, 62]. The transverse strains from the baseline simulation are consistent with these observations and are in good agreement with the MR tagging experiments [1].

Comparing the cVclKO active contraction simulations to the control results reveals systolic strain trends similar to those observed experimentally [1]. The KO strain in the fiber direction remains approximately unchanged as compared to the control simulation. The result confirms the observation that deletion of Vcl from cardiac myocytes does not interfere with their ability to contract at the studied age prior to the onset of heart failure. The predicted result is consistent with previous experimental observations that demonstrate no change in systolic fiber strain *in vivo* [1]; additionally, preliminary studies in isolated papillary muscles of heterozygous global cVclKO mice show no difference in isometric fiber tension development.

The increased lattice spacing of the KO mice results in decreased radial and cross-fiber strains at end-systole as predicted in the structural analysis of crossbridge orientation. The difference in radial strain between the two genotypes is smaller at the epicardium than the endocardium, coinciding with MR tagging observations. The

experimental data seems to show that the transmural variation of the radial strain reverses when Vcl is removed; while the KO simulation does not reflect this trend, the transmural variation does flatten out slightly with the increased transverse crossbridge stiffness. The altered stress distribution did not have a large effect on the cross-fiber shortening. Small increases at the mid-wall and epicardium were observed, which is consistent with the experimental results, but the magnitude of the changes is much smaller. When comparing the results of the simulation to the experimental observations, it is important to keep in mind the large standard deviations in the experimental data that were not indicated on the graphs.

Position vectors for the Gauss points at the endocardium and epicardium were utilized to determine the amount of wall thickening during contraction. The KO simulation exhibited less thickening as compared to the control, which is also consistent with experimental measurements [1]. During systole, radial thickening of the LV wall is important for blood ejection [63]; therefore, the model predicts that Vcl deletion may reduce the LV's ability to properly eject. Previous studies have shown that the ejection fraction of the cVclKO hearts were in fact slightly lower as compared to the control hearts [1].

There are several limitations to the analyses and modeling approaches employed in the present study. First, the fiber angles included throughout the mesh were only measured experimentally at the equator because of the difficulty associated with obtaining these measurements throughout the heart; the transmural variation in fiber angle at the apex is most likely very different than that at the equator. Second, the strain dependence of the crossbridge analysis and fiber angle dispersions were not

taken into account; in the contracting heart, the deformation at any given time point will alter the lattice spacing and fiber angle dispersion as the LV proceeds from end-diastole to end-systole. Because of the large strains currently observed at the endocardium, accounting for the strain dependence may significantly alter the stress ratios and exacerbate the genotypic differences at the endocardium such that they coincide with the MR tagging results. Finally, an oversimplification of the model may have affected the accuracy of the predictions. Because the sheet structure of the cardiomyocytes was not considered, only accounting for the fiber dispersion is appropriate for the present study; however, the dispersion of the sheet angles was not accounted for, thereby limiting the accuracy of the force distribution calculations. Also, the myocardium was modeled as a transversely isotropic material while a transversely orthotropic model may have offered more insight into the effects of Vcl deletion on fiber and sheet function.

The results of the present study are an important step in understanding the mechanistic link between the structural alterations and ventricular dysfunction associated with Vcl deletion prior to the onset of heart failure. Despite the differences in the magnitudes of the strain changes between the experimental groups, the finite element model still provided valuable qualitative insight into the regional mechanical effects associated with Vcl deletion from cardiac myocytes and was able to recapitulate key mechanical differences observed experimentally. The increased lattice spacing of the cVclKO had a negligible effect on fiber strain and reduced the amount of regional wall thickening. While the predicted differences between KO and control are consistent with the MR tagging experiments in mice [1], the magnitudes of

the changes in the simulation caused by the removal of Vcl are substantially different than the measured values. This could be because the change in sarcomeric structure is not the only mechanism responsible for the altered ventricular function or because the model was not sophisticated enough to accurately capture the complexities of the structural changes.

3.5 ACKNOWLEDGEMENTS

Chapter 3, in part, is currently being prepared for submission for publication of the material. Chuang J; Janssen MS; Tangney J; Liao P; Ross RS; McCulloch AD; Omens JH. "The Role of Vinculin in Active Fiber and Sheet Mechanics." The thesis author was the secondary investigator and author of this material.

Chapter 4

Summary and Conclusions

Electron microscopy was utilized to study the structural changes associated with Vcl deletion in murine hearts prior to the onset of heart failure. The EM studies revealed significant changes in the sarcomeric structure of cVclKO hearts. The myofilament lattice spacing was significantly larger in the KO hearts fixed in the end-diastolic state; despite a similar trend being observed in the barium-contracted hearts, no statistical significance was reported. The increased lattice spacing in the KO as compared to the controls is believed to significantly affect the crossbridge orientation, which in turn would affect force generation. It was hypothesized that increasing the lattice spacing would increase the crossbridge angle and subsequently, the transverse stiffness of the crossbridge in the KO. These changes could explain the altered systolic strain patterns detailed in previous experiments [1].

To test the hypothesized mechanism, a finite element model of a murine LV was created. The effects of the altered lattice geometry and fiber angle dispersion were accounted for in the model. Active contraction simulations produced systolic strain trends qualitatively similar to those observed in MR tagging experiments of cardiac tissue [1]; the increased crossbridge stiffness of the KO resulted in reduced systolic radial strain but did not affect the fiber shortening of the cardiac myocytes.

While the model trends between the two groups were similar, the magnitude of the change in strains was not consistent with experimental measurements, suggesting that the change in lattice spacing may not be the sole reason for the ventricular dysfunction associated with Vcl disruption. It is possible that the model was too simplistic to capture all of the nuances associated with Vcl deletion, but more simulations and experiments are required to further examine this mechanism. The results of the present study in conjunction with experimental measurements suggest that Vcl can influence myofilament architecture and systolic force generation in a direction-dependent manner.

References

1. Chuang JS. 2010. "The Role of Costameric Proteins in Cardiac Force Transmission and Signaling". Dissertation, University of California, San Diego: Bioengineering.

2. Lieber RL, Burkholder TJ, "Musculoskeletal Soft Tissue Mechanics" in *Biomedical Engineering Fundamentals*. J.D. Bronzino, 3rd ed. 2006, Boca Raton: Taylor & Francis Group. p. 48.1-48.13.

3. Hiroyuki M, Seidman J, Seidman CE. 2005. "Genetic causes of human heart failure". *J Clin Invest*. **115**(3): 518-526.

4. Millman BM. 1998. "The Filament Lattice of Striated Muscle". *Physiological Reviews*. **78**(2): 359-391.

5. Ervasti JM. 2003. "Costameres: the Achilles' Heel of Herculean Muscle". *J Biol Chem*. **278**(16): 13591-13594.

6. Sharp WW, Simpson DG, Borg TK, Samarel AM, Terracio L. 1997. "Mechanical forces regulate focal adhesion and costamere assembly in cardiac myocytes". *Am J Physiol Heart Circ Physiol*. **273**: H546-H556.

7. Clark KA, McElhinny AS, Beckerle MC, Gregorio CC. 2002. "Striated muscle cytoarchitecture: an intricate web of form and function". *Annu. Rev. Cell Dev. Biol*. **18**: 637-706.

8. Samarel AM. 2005. "Costomeres, focal adhesions, and cardiomyocyte mechanotransduction". *Am J Physiol Heart Circ Physiol*. **289**: H2291 - H2301.

9. Danowski B, Imanaka-Yoshida K, Sanger J. 1992. "Costameres are sites of force transmission to the substratum in adult rat cardiomyocytes". *J Cell Biol*. **118**: 1411-1420.

10. Rudiger M, Korneeva N, Schwienbacher C, Weiss EE, Jockusch BM. 1998. "Differential actin organization by vinculin isoforms: implications for cell type-specific microfilament anchorage.". *FEBS Lett*. **431**: 49-54.

11. Schlaepfer DD, Hunter T. 1996. "Signal transduction from the extracellular matrix - a role for the focal adhesion protein-tyrosine kinase FAK". *Cell Struct Funct*. **21**: 445 - 450.

12. Hildebrand JD, Schaller MD, Parsons JT. 1993. "Identification of sequences required for the efficient localization of the focal adhesion kinase, pp125FAK, to cellular focal adhesions". *J Cell Biol*. **123**: 993 - 1005.

13. Zemljic-Harpf AE, Ponrartana S, Avalos RT, Jordan MC, Roos KP, Dalton ND, Phan VQ, Adamson ED, Ross RS. 2004. "Heterozygous Inactivation of the Vinculin Gene Predisposes to Stress-Induced Cardiomyopathy". *American Journal of Patholgy*. **165**(3): 1033 - 1044.

14. Zemljic-Harpf AE, Miller JC, Henderson SA, Wright AT, Manso AM, Elshrif L, Dalton ND, Thor AK, Perkins GA, McCulloch AD, Ross RS. 2007. "Cardiac-Myocyte-Specific Excision of the Vinculin Gene Disrupts Cellular Junctions, Causing Sudden Death or Dilated Cardiomyopathy". *Molecular and Cellular Biology*. **27**(21): 7522 - 7537.

15. Palmer SM, Playford MP, Craig SW, Schaller MD, Campbell SL. 2009. "Lipid Binding to the Tail Domain of Vinculin: Specificity and the Role of the N and C Termini". *Journal of Biological Chemistry*. **284**(11): 7223 - 7231.

16. Goldmann WH, Galneder R, Ludwig M, Xu W, Adamson ED, Wang N, Ezzell RM. 1998. "Differences in elasticity of vinculin-deficient F9 cells measured by magnetometry and atomic force microscopy". *Exp. Cell Res.* **239**(2): 235 - 242.

17. Hoshijima M. 2006. "Mechanical stress-strain sensors embedded in cardiac cytoskeleton: Z disk, titin, and associated structures". *Am J Physiol Heart Circ Physiol*. **290**: H1313 - H1325.

18. Pearson JT, Shirai M, Ito H, Tokunaga N, Tsuchimochi H, Nishiura N, Schwenke DO, Ishibashi-Ueda H, Akiyama R, Mori H, Kangawa K, Suga H, Yagi N. 2004. "In Situ Measurements of Crossbridge Dynamics and Lattice Spacing in Rat Hearts by X-Ray Diffraction: Sensitivity to Regional Ischemia". *Circulation*. **109**(24): 2976-2979.

19. Irving TC, Konhilas J, Perry D, Fischetti R, de Tombe PP. 2000. "Myofilament lattice spacing as a function of sarcomere length in isolated rat myocardium". *Am J Physiol Heart Circ Physiol*. **279**(5): H2568-H2573.

20. Yagai N, Okuyama H, Toyota H, Araki J, Shimizu J, Iribe G, Nakamura K, Mohri S, Tsujioka K, Suga H, Kajiya F. 2004. "Sarcomere-length dependence of lattice volume

and radial mass transfer of myosin cross-bridges in rat papillary muscle". *Eur. J Physiol*. **448**(2): 153-160.

21. Farman GP, Allen EJ, Gore D, Irving TC, de Tombe PP. 2007. "Interfilament Spacing is Preserved during Sarcomere Length Isometric Contractions in Rat Cardiac Trabeculae". *Biophysical Journal*. **92**(9): L73-L75.

22. Martin DA, Adhikari BB, Regnier M, Gu J, Xu S, Yu LC. 2004. "Response of Equatorial X-Ray Reflections and Stiffness to Altered Sarcomere Length and Myofilament Lattice Spacing in Relaxed Skinned Cardiac Muscle". *Biophysical Journal*. **86**(2): 1002-1011.

23. Cecchi G, Bagni MA. 1994. "Myofilament lattice spacing affects tension in striated muscle". *News Physiol. Sci*. **9**: 3-7.

24. McCulloch AD, "Cardiac Biomechanics" in *Biomedical Engineering Fundamentals*. J.D. Bronzino, 3rd ed. 2006, Boca Raton: Taylor & Francis Group. p. 54.1-54.27.

25. Geyer H, Caracciolo G, Abe H, Wilansky S, Carerj S, Gentile F, Nesser H, Khandheria B, Narula J, Sengupta PP. 2010. "Assessment of myocardial mechanics using speckle tracking echocardiography: fundamentals and clinical applications". *Journal of the American Society of Echocardiography*. **23**(4): 351-369.

26. Garot J, Bluemke DA, Osman NF, Rochitte CE, McVeigh ER, Zerhouni EA, Prince JL, Lima JA. 2000. "Fast Determination of Regional Myocardial Strain Fields From Tagged Cardiac Images Using Harmonic Phase MRI". *Circulation*. **101**: 981-988.

27. McCulloch AD, Sung D, Wilson JM, Pavelec RS, Omens JH. 1998. "Flow-function relations during graded coronary occlusions in the dog: effects of transmural location and segment orientation". *Cardiovascular Research*. **37**(3): 636-645.

28. Franco F, Dubois SK, Peshock RM, Shohet RV. 1998. "Magnetic Resonance Imaging Accurately Estimates LV Mass in a Transgenic Mouse Model of Cardiac Hypertrophy". *Am J Physiol*. **274**(2): H679-H683.

29. Wiesmann F, Frydrychowicz A, Rautenberg J, Illinger R, Rommel E, Haase A, Neubauer S. 2002. "Analysis of right ventricular function in healthy mice and a murine model of heart failure by *in vivo* MRI". *Am J Physiol Heart Circ Physiol*. **283**(3): H1065-H1071.

30. Costandi PN, Frank LR, McCulloch AD, Omens JH. 2006. "Role of diastolic properties in the transition to failure in a mouse model of the cardiac dialation". *Am J Physiol Heart Circ Physiol*. **291**(6): H2971-H2979.

31. Ross AJ, Yang Z, Berr SS, Gilson WD, Petersen WC, Oshinski JN, French BA. 2002. "Serial MRI evaluation of cardiac structure and function in mice after reperfused myocardial infarction". *Magnetic Resonance in Medicine*. **47**(6): 1158-1168.

32. Zhong J, Liu W, Yu X. 2009. "Transmural myocardial strain in mouse: quantification of high-resolution MR tagging using harmonic phase (HARP) analysis". *Magn Reson Med*. **61**: 1368-1373.

33. Young AA, Axel L. 1992. "Three-dimensional motion and deformation in the heart wall: estimation from spatial modulation of magnetization - a model-based approach". *Radiology*. **185**: 241-247.

34. Heijman E, Strijkers GF, Habets J, Janssen B, Nicolay K. 2004. "Magnetic Resonance Imaging of Regional Cardiac Function in the Mouse". *MAGMA*. **17**: 170-178.

35. McVeigh ER. 1996. "MRI of Myocardial Function: Motion Tracking Techniques". *Magnetic Resonance Imaging*. **14**(2): 137-150.

36. Huisman RM, Elzinga G, Westerhof N, Sipkema P. 1980. "Measurement of left ventricular wall stress". *Cardiovascular Research*. **14**(3): 142-153.

37. Kerckhoffs RCP, Narayan SM, Omens JH, Mulligan LJ, McCulloch AD. 2008. "Computational Modeling for Bedside Application". *Heart Fail. Clin*. **4**(3): 371-378.

38. Kerckhoffs RCP, McCulloch AD, Omens JH, Mulligan LJ. 2007. "Effect of Pacing Site and Infarct Location on Regional Mechanics and Global Hemodynamics in a Model Based Study of Heart Failure". *Functional Imaging and Modeling of the Heart: Lecture Notes in Computer Science*. **4466**: 350-360.

39. Hayashi T, Martone ME, Yu Z, Thor A, Doi M, Holst MJ, Ellisman MH, Hoshijima M. 2009. "Three-dimensional electron microscopy reveals new details of membrane systems for Ca2+ signaling in the heart". *J Cell Sci*. **122**(Pt 7): 1005-1013.

40. Jynge P, Hearse DJ, Feuvray D, Mahalu W, Cankovic-Darracott S, O'Brien K, Braimbridge MV. 1981. "The St. Thomas' hospital cardioplegic solution: a characterization in two species". *Scand J Thorac Cardiovasc Surg Suppl*. **30**: 1-28.

41. Munch DF, Comer HT, Downey JM. 1980. "Barium contracture: a model for systole". *Am J Physiol Heart Circ Physiol*. **239**(3): H438-H442.

42. Chen J, Liu W, Zhang H, Lacy L, Yang X, Song S, Wickline SA, Yu X. 2005. "Regional ventricular wall thickening reflects changes in cardiac fiber and sheet structure during contraction: quantification with diffusion tensor MRI". *Am J Physiol Heart Circ Physiol*. **289**: H1898-H1907.

43. JEOL Ltd. 2011. "Preparation of biological specimens for Electron Microscopy: for TEM". Available from: http://www.jeolusa.com/RESOURCES/ElectronOptics/DocumentsDownloads/tabid/320/Default.aspx?EntryId=560.

44. Hayat MA, *Principles and Techniques of Electron Microscopy: Biological Applications*. 4th ed. 2000, Cambridge: Cambridge University Press.

45. Sakai T. 1980. "Relation between Thickness and Interference Colors of Biological Ultrathin Section". *J Electron Microsc*. **29**(4): 369-375.

46. Mastronarde DN. 2005. "Automated electron microscope tomography using robust prediction of specimen movements". *J. Struct. Biol.* **152**: 36-51.

47. Molina T. 2011. "SerialEM tutorial page for IVEM users". Available from: https://confluence.crbs.ucsd.edu/display/ncmir/SerialEM+tutorial+page+for+IVEM+users.

48. Matsubara I, Millman BM. 1974. "X-ray diffraction patterns from mammalian heart muscle". *J. Mol. Biol*. **82**: 527-536.

49. Rodriguez EK, Omens JH, Waldman LK, McCulloch AD. 1993. "Effect of residual stress on transmural sarcomere length distributions in rat left ventricle". *Am J Physiol*. **264**(4 Pt. 2): H1048-56.

50. Schoenberg M. 1980. "Geometrical Factors Influencing Muscle Force Development: I. The Effect of Filament Spacing Upon Axial Forces". *Biophysical Journal*. **30**: 51-68.

51. Williams CD, Regnier M, Daniel TL. 2010. "Axial and Radial Forces of Cross-Bridges Depend on Lattice Spacing". *PLoS Computational Biology*. **6**(12): 1-10.

52. Julian FJ, Moss RL, Sollins MR. 1978. "The mechanism for vertebrate striated muscle contraction". *Circ Res*. **42**: 2-14.

53. Rayment I, Holden HM, Whittaker M, Yohn CB, Lorenz M, Holmes KC, Milligan RA. 1993. "Structure of the Actin-Myosin Complex and Its Implications for Muscle Contraction". *Science*. **261**(5117): 58-65.

54. Sonnenblick EH, Skelton CL. 1974. "Reconsideration of the Ultrastructural Basis of Cardiac Length-Tension Relations". *Circ Res*. **35**: 517-526.

55. Coppola BA. 2008. "Effects of Asynchrony and Anatomic Structure on Left Ventricular Mechanics". Dissertation, University of California, San Diego: Bioengineering.

56. Usyk TP, Mazhari R, McCulloch AD. 2000. "Effect of Laminar Orthotropic Myofiber Architecture on Regional Stress and Strain in the Canine Left Ventricle". *Journal of Elasticity*. **61**: 143-164.

57. Karlon WJ. 1998. "Influence of Myocardial Fiber Organization on Ventricular Function". Dissertation, University of California, San Diego: Bioengineering.

58. Guccione JM, Costa KD, McCulloch AD. 1995. "Finite element stress analysis of left ventricular mechanics in the beating dog heart". *J Biomech*. **28**(10): 1167-77.

59. Guccione JM, Waldman LK, McCulloch AD. 1993. "Mechanics of active contraction in cardiac muscle". *J Biomech Eng*. **115**(1): 72-90.

60. Schoenberg M. 1980. "Geometrical Factors Influencing Muscle Force Development: II. Radial Forces". *Biophysical Journal*. **30**: 69-78.

61. Costa KD, Holmes JW, McCulloch AD. 2001. "Modelling cardiac mechanical properties in three dimensions". *Phil. Trans. R. Soc. Lond. A*. **359**: 1233-1250.

62. Rademakers FE, Rogers WJ, Guier WH, Hutchins GM, Siu CO, Weisfeldt ML, Weiss JL, Shapiro EP. 1994. "Three-dimension Strain Analysis by NMR Tagging". *Circulation*. **89**: 1174-1182.

63. Dumesnil JG, Shoucri RM. 1991. "Quantitative relationships between left ventricular ejection and wall thickening and geometry". *J Appl Physiol*. **70**: 48-54.

Appendix A

Constant Volume Analysis of cVclKO Mice

Table A.1: Analysis of lattice spacing measurements in end-diastolic hearts assuming constant lattice volume to determine whether the observed differences were attributed to Vcl deletion or different SL measurements

Mouse # 5506: End-Diastolic Heart				
Mouse ID	**SL**	**Meas. Control M-M LS**	**Calc. KO M-M LS**	**% Diff**
5507	1.90	30.05	31.84	5.9%
5510	1.87	31.34	32.02	2.2%
5516	2.19	31.08	29.62	-4.7%

Mouse # 5511: End-Diastolic Heart				
Mouse ID	**SL**	**Meas. Control M-M LS**	**Calc. KO M-M LS**	**% Diff**
5507	1.90	30.05	33.06	10.0%
5510	1.87	31.34	33.26	6.1%
5516	2.19	31.08	30.76	-1.1%

Mouse # 5517: End-Diastolic Heart				
Mouse ID	**SL**	**Meas. Control M-M LS**	**Calc. KO M-M LS**	**% Diff**
5507	1.90	30.05	31.30	4.2%
5510	1.87	31.34	31.49	0.5%
5516	2.19	31.08	29.12	-6.3%

Table A.2: Analysis of lattice spacing measurements in barium-contracted hearts assuming constant lattice volume to determine whether the observed differences were attributed to Vcl deletion or different SL measurements

Mouse # 8214: Barium-Contracted Heart				
Mouse ID	**SL**	**Meas. Control M-M LS**	**Calc. KO M-M LS**	**% Diff**
8209	1.42	31.79	39.59	24.5%
8210	1.43	34.70	39.40	13.5%
8212	1.64	32.22	36.74	14.0%

Mouse # 8215: Barium-Contracted Heart				
Mouse ID	**SL**	**Meas. Control M-M LS**	**Calc. KO M-M LS**	**% Diff**
8209	1.42	31.79	39.17	23.2%
8210	1.43	34.70	38.99	12.4%
8212	1.64	32.22	36.36	12.8%

Mouse # 8216: Barium-Contracted Heart				
Mouse ID	**SL**	**Meas. Control M-M LS**	**Calc. KO M-M LS**	**% Diff**
8209	1.42	31.79	34.62	8.9%
8210	1.43	34.70	34.46	-0.7%
8212	1.64	32.22	32.13	-0.3%

Appendix B

MATLAB Script for Calculating Fiber Force, Radial Force, and Radial to Fiber Force Ratio using Geometrical Analysis

```
%%variables that can be changed: theta, phi, gamma, k, x0%%

clear all
alpha=45; %Angle formed by S1 and actin (deg)
gamma=45; %Assumed azimuthal position of crossbridge - slew (deg)
l1=16; %Length of S1 region (nm)
l2=40; %Length of S2 region (nm)
WT_convFact = 0.0131; %Normalized control lattice spacing from EM study
KO_convFact = 0.0149;  %Normalized KO lattice spacing from EM study
SL_avg = 1460; %Average SL in nm
LS_WT=SL_avg*WT_convFact %Control center-to-center lattice spacing (nm)
LS_KO=SL_avg*KO_convFact %KO center-to-center lattice spacing (nm)
k=2; %Spring constant (pN/nm)
x0=20; %Spring reference length (nm)

%Solving for Z'%
theta=60; %Azimuthal location of S2 origin on myosin (deg)
phi=60; %Azimuthal location of actin binding site (deg)
ra=3; %Radius of actin (nm)
rm=5.5; %Radius of myosin (nm)
xa=ra*sind(phi); %Height of actin binding site (nm)
xm=rm*sind(theta); %Height of S2 attachment site (nm)
ym=xm-xa; %Height of Z triangle (nm)
a=xa/tand(phi); %Difference between LS and actin binding site projected onto LS (nm)
b=xm/tand(theta); %Difference between LS and S2 attachment site projected onto LS (nm)
ss_WT=LS_WT-a-b; %Control base of Z triangle in nm (surf-to-surf)
ss_KO=LS_KO-a-b; %KO base of Z triangle in nm (surf-to-surf)
Z_WT=sqrt((ss_WT)^2+(ym)^2) %Control Z' distance in Schoenberg model (nm)
Z_KO=sqrt((ss_KO)^2+(ym)^2) %KO Z' distance in Schoenberg model (nm)
epsilon_WT=atand(ym/ss_WT) %Angle of elevation for Z_WT wrt lattice spacing (deg)
epsilon_KO=atand(ym/ss_KO) %Angle of elevation for Z_KO wrt lattice spacing (deg)

%Solving for Angle Between S2 and Myosin Filament%
M_WT=Z_WT; %Control surface-to-surface spacing between actin and myosin (nm)
M_KO=Z_KO; %KO surface-to-surface spacing between actin and myosin (nm)
y1=l1*sind(alpha); %Distance between S1-S2 junction and actin (nm)
y2_WT=M_WT-y1; %Control distance between S1-S2 junction and myosin (nm)
y2_KO=M_KO-y1; %KO distance between S1-S2 junction and myosin (nm)

beta_WT=asind(y2_WT/l2); %Control angle between S2 and myosin filament (deg)
```

```
X_WT=l2*cosd(beta_WT)-l1*cosd(alpha); %Control horiz distance from S2 attachment site to actin binding site projected onto myosin (nm)


horiz_dist=l2*cosd(beta_WT); %Horiz. distance from S2 attachment site to S1-S2 junction projected onto myosin (nm)

beta_KO=atand(y2_KO/horiz_dist); %KO angle between S2 and myosin filament (deg)
l2_KO=y2_KO/sind(beta_KO) %S2 length in KO (nm)
X_KO=l2_KO*cosd(beta_KO)-l1*cosd(alpha); %KO horiz distance from S2 attachment site to actin binding site projected onto myosin (nm)

%Solving for Fiber Force, Radial Force, and Ratio of Radial:Fiber%
delta_WT=phi-gamma-epsilon_WT; %Control crossbridge angle of rotation (deg)
delta_KO=phi-gamma-epsilon_KO; %KO crossbridge angle of rotation (deg)

Fab_WT=k*(l2-x0); %Control force in S2 (pN)
Fab_KO=k*(l2_KO-x0); %KO force in S2 (pN)

F_radial_WT=Fab_WT*(Z_WT*cosd(epsilon_WT)-l1*sind(alpha)*cosd(delta_WT+epsilon_WT))/l2
%Control radial force (pN)
F_radial_KO=Fab_KO*(Z_KO*cosd(epsilon_KO)-
l1*sind(alpha)*cosd(delta_KO+epsilon_KO))/l2_KO %KO radial force (pN)

F_fiber_WT=Fab_WT*(X_WT+l1*cosd(alpha))/l2 %Control fiber force (pN)
F_fiber_KO=Fab_KO*(X_KO+l1*cosd(alpha))/l2_KO %KO fiber force (pN)

Kr_WT=(Z_WT*cosd(epsilon_WT)-
l1*sind(alpha)*cosd(delta_WT+epsilon_WT))/(X_WT+l1*cosd(alpha)) %Control ratio
Kr_KO=(Z_KO*cosd(epsilon_KO)-
l1*sind(alpha)*cosd(delta_KO+epsilon_KO))/(X_KO+l1*cosd(alpha)) %KO ratio

percentChange = ((Kr_KO-Kr_WT)/Kr_WT)*100
```

Appendix C

MATLAB Script for Calculating the Effect of Fiber Dispersion on the Stress Scaling Coefficients

```
clear all

k1 = 1;    %Input k1 value, fiber direction scaling factor
k2 = 0.0991; %Input k2 value, radial direction scaling factor (k2=0.1651 for KO)
k3 = k2;    %Myocardium modeled as transversely isotropic material

t = 1;      %Input fiber stress

a = -pi()/2; b = pi()/2;
x = a:pi()/180:b;
kappa_12=5.307;   %For angular fiber dispersion of 12 degrees

%Evaluate Probability Density Function
VonMises_phi=2*exp(kappa_12*cos(2*x))/(2*pi()*besseli(0,kappa_12)); %about radial axis
VonMises_theta=2*exp(kappa_12*cos(2*x))/(2*pi()*besseli(0,kappa_12));   %about x-fiber axis

integral=trapz(x,VonMises_phi);   %verify that area under curve is 1

T_local = [k1*t 0 0; 0 k2*t 0; 0 0 k3*t];   %Input local stress tensor

tempT_phi = zeros(3,3);
tempT_theta=zeros(3,3);

for phi = a:pi()/180:b        %Accounting for fiber dispersion about radial axis

   degree = pi()/180;  %1 degree increments
   pt1 = round(phi/degree +91);
   pt2 = round(phi/degree +92);
   if pt2==182
      break
   end

   VM_low = VonMises_phi(pt1);
   VM_high = VonMises_phi(pt2);
   intf=((VM_high+VM_low)/2)*degree;  %Evaluate area under PDF over 1 deg interval using
                                        midpoint

   R_phi = [ cos(phi) sin(phi) 0; -sin(phi) cos(phi) 0; 0 0 1]; %Evaluate R at phi value
   Rt_phi = R_phi';  %Evaluate R-transpose at phi value

   intT = R_phi*T_local*Rt_phi*intf;          %Calculate stress components at current phi value
```

```
    tempT_phi = tempT_phi + intT;  %Calculate new total stress components

end

T_star=tempT_phi                    %Output stress distribution after accounting for radial dispersion
T_star(3,3)=0;      %Reset radial component to 0

for theta = a:pi()/180:b    %Accounting for fiber dispersion about x-fiber axis

    degree = pi()/180;  %1 degree increments
    pt1 = round(theta/degree +91);
    pt2 = round(theta/degree +92);
    if pt2==182
        break
    end

    VM_low2 = VonMises_theta(pt1);
    VM_high2 = VonMises_theta(pt2);
    intf_theta=((VM_high2+VM_low2)/2)*degree;       %Calculate area under von Mises over 1deg
                                                     interval using midpoint

    R_theta = [ cos(theta) 0 sin(theta); 0 1 0; -sin(theta) 0 cos(theta)]; %Evaluate R at theta for control
    Rt_theta = R_theta';  %Evaluate R-transpose at theta for control

    intT_theta = R_theta*T_star*Rt_theta*intf_theta;     %Calculate stress components at theta for
control
    tempT_theta = tempT_theta + intT_theta;    %Calculate new total stress components for control
end

T_tissue=tempT_theta;
trans_ratio=T_tissue(2,2)/T_tissue(1,1) %Calculate new transverse:axial stress ratio that accounts for
                                         geometrical effects and fiber dispersion effects
```